https://doi.org/10.5194/egusphere-2026-6769
Preprint. Discussion started: 20 November 2026
© Author(s) 2026. CC BY 4.0 License.

Contrasting vertical ozone evolution between coastal and inland sites within a subtropical coastal city: roles of photochemistry and transport during typhoon-influenced weather

Shaojie Jiang[1, 2, 3, #], Xinlei Ge[1, 4, #], Dongyang Nie[2, 5, #], Xiangpeng Huang[2, 6], Wei Zheng[2], Honglong Yang[7], Yaying Wang[2], Yan Yang[2], Weifeng Su[2], Linqiang Ma[2], Tianzeng Chen[8], Yanli Zhang[9], Shutong Jiang[10], Qiyuan Wang[11], Junfeng Wang[1], Chanfang Liu[5], Lei Zhu[2], Zhenzhong Zeng[2], Tzung-May Fu[2], Xin Yang[2], Jianhuai Ye[2, 3, *]

[1] Jiangsu Key Laboratory of Atmospheric Environment Monitoring and Pollution Control, School of Environmental Science and Engineering, Nanjing University of Information Science and Technology, Nanjing 210044, China

[2] State Key Laboratory of Soil Pollution Control and Safety, School of Environmental Science and Engineering, Southern University of Science and Technology, Shenzhen 518055, China

[3] Guangdong Provincial Observation and Research Station for Coastal Atmosphere and Climate of the Greater Bay Area, Shenzhen 518055, China

[4] School of Energy and Environment, Southeast University, Nanjing 211189, China

[5] Shenzhen Ecological and Environmental Monitoring Centre of Guangdong Province, Shenzhen 518049, China

[6] The Jiangsu Key Laboratory of Electronic Waste and New Energy Solid Waste Resource Utilization, School of Resources and Environmental Engineering, Jiangsu University of Technology, Changzhou 213001, China

[7] Shenzhen National Climate Observatory, Meteorological Bureau of Shenzhen Municipality, Shenzhen 518040, China

[8] State Key Joint Laboratory of Environment Simulation and Pollution Control, Research Center for Eco-Environmental Sciences, Chinese Academy of Sciences, Beijing 100085, China

[9] State Key Laboratory of Advanced Environmental Technology, Guangzhou Institute of Geochemistry, Chinese Academy of Sciences, Guangzhou, China

[10] Soarability Pte. Ltd., Singapore 409051, Singapore

[11] Key Laboratory of Aerosol Chemistry and Physics, Chinese Academy of Sciences Institute of Earth Environment, Xi'an 710061, China

[#] These authors contributed equally to the study.

Correspondence to: Jianhuai Ye (yejh@sustech.edu.cn), ORCID 0000-0002-9063-3260

https://doi.org/10.5194/egusphere-2026-6769
Preprint. Discussion started: 20 November 2026
© Author(s) 2026. CC BY 4.0 License.



Abstract. Interactions between coastal and regional circulations shape air quality in coastal regions, yet their combined influence on ozone (O_3) formation and distribution remains poorly understood. Here we integrated unmanned aerial vehicle profiles, tower observations, and observation-based atmospheric chemistry modelling to examine these processes during typhoon-influenced weather in a representative coastal city in South China. Measurements at coastal and inland sites within the same city revealed contrasting meteorological conditions, precursor abundances, and O_3 evolution. Stronger typhoon influence coincided with warmer, drier conditions and approximately doubled total volatile organic compound concentrations, leading to enhanced net photochemical O_3 production. At the coastal site, O_3 concentration evolution was associated with the interplay between land–sea breezes and regional flow, a pattern observed repeatedly during the typhoon-influenced days. At the inland site, O_3 remained consistently higher aloft, with low surface concentrations likely resulting from chemical consumption and dry deposition to vegetation. Model simulations showed that local gas-phase chemistry accounted for 59% and 33% of the observed rapid O_3 increases at the coastal and inland sites, indicating substantial roles for vertical redistribution and regional transport. Sensitivity analyses indicated that reductions in volatile organic compounds suppressed O_3 production at both sites, although the relative importance of individual precursors differed between the sites. Overall, this study highlights that the same regional weather system can generate distinct O_3 evolution within one urban region. Effective mitigation requires local precursor controls coordinated with regional emission reductions and vertically resolved observations that identify changes in air-mass influence and elevated O_3 layers.

https://doi.org/10.5194/egusphere-2026-6769
Preprint. Discussion started: 20 November 2026
© Author(s) 2026. CC BY 4.0 License.

1. Introduction

Tropospheric ozone (O_3) is a major air pollutant that adversely affects human health and contributes to climate warming (Monks et al., 2015; Lu et al., 2020). Despite substantial reductions in many primary air pollutants in China, summertime O_3 has increased markedly during the past decade and remains a major challenge for air-quality management (Li et al., 2020; W. Wang et al., 2022). O_3 pollution is particularly complex in South China, where high levels of anthropogenic and biogenic volatile organic compounds (VOCs), strong solar radiation, and regional transport favour active photochemistry (Zheng et al., 2009; Shao et al., 2009; Wang et al., 2010; Xue et al., 2016; He et al., 2019; Liu et al., 2025).

The chemical processes governing O_3 formation are further modulated by coastal circulation and rapidly evolving synoptic meteorology. Tropical cyclones are recurrent disturbances across tropical and subtropical coastal regions. In South China, their peripheral circulations can simultaneously alter temperature, solar radiation, boundary-layer structure, precursor distributions, and regional pollutant transport (Li et al., 2022; Ouyang et al., 2022; N. Wang et al., 2022; Deng et al., 2019). For instance, Guangdong Province in the Pearl River Delta experienced an average of around three landfalling tropical cyclones per year during 1980–2020 (Ning et al., 2023). During the 2015–2020 warm seasons, tropical cyclones at midrange distances (700–4500 km) from the Pearl River Delta accounted for around 80% of persistent O_3 exceedances (Hu et al., 2023). However, the magnitude and mechanisms of tropical-cyclone impacts on O_3 depend strongly on cyclone position, track, and stage of development (Huang et al., 2005; Yang et al., 2012; Jiang et al., 2015; Wang et al., 2024; Qi et al., 2024). Understanding O_3 pollution under such conditions therefore requires resolving both chemical production and atmospheric transport rather than treating either process in isolation.

A major difficulty for elucidating O_3 formation is that surface O_3 reflects processes occurring both near the surface and aloft. Conventional surface measurements can characterize local pollution evolution but provide limited information on O_3 and precursor distributions above the ground. Previous observations have revealed substantial vertical variability in O_3 production and chemical sensitivity within the lower troposphere (Hu et al., 2024), and lidar and ozonesonde measurements have shown strong synoptic control of elevated O_3 layers and regional transport (Lin et al., 2021; Liao et al., 2024). However, vertical O_3 structures alone cannot uniquely diagnose the underlying processes across locations and under different atmospheric conditions. Similar vertical concentration patterns can arise from different combinations of horizontal transport, vertical exchange, boundary-layer development, local coastal circulation, and photochemical production. Distinguishing among these processes therefore requires simultaneous information on the vertical distributions of both atmospheric composition and meteorological structure.

Recent advances in unmanned aerial vehicle (UAV) platforms have expanded atmospheric observational capabilities beyond conventional surface networks. UAVs provide a flexible means of measuring atmospheric composition and meteorological structure in the lower troposphere at high spatial and temporal resolution, capturing variations that conventional ground-based monitoring networks cannot readily resolve (Wu et al., 2021; Guimarães et al., 2020; Ma et al., 2021; Ye et al., 2021; Batista et al., 2019; Ye et al., 2022; Jiang et al., 2024; Li et al., 2025; Chen et al., 2026). In addition, O_3 formation can differ markedly among locations within the same city because of variations in emission sources, local meteorological conditions, and regional influences. Simultaneous vertically resolved chemical and meteorological measurements at multiple locations are therefore essential for developing a comprehensive understanding of O_3 formation across the city.

Here, we used vertically resolved observations from two field campaigns in a representative coastal city in South China, conducted in August-September 2022 and May-June 2023, to investigate how photochemistry and atmospheric transport shape O_3 evolution under contrasting meteorological conditions. The 2023 campaign captured the outer-circulation influence of Super Typhoon Mawar and included simultaneous observations at an inland tower, allowing us to examine concurrent

https://doi.org/10.5194/egusphere-2026-6769
Preprint. Discussion started: 20 November 2026
© Author(s) 2026. CC BY 4.0 License.

changes in precursor abundance, photochemical activity, local and regional flow, and vertical O_3 structure across the coastal and inland sites. Observations from the longer 2022 campaign provided additional context for pathway-dependent pollutant contrasts outside periods of direct tropical-cyclone influence. Air-mass trajectory analysis and observation-constrained chemical modelling were further used to characterize regional transport and assess the role of local gas-phase chemistry in the observed O_3 evolution. Together, these observations and analyses link differences in coastal and inland O_3 evolution to changes in the vertical distribution of precursors and meteorological parameters, providing insights into effective O_3 mitigation measures in coastal regions.

2. Methods

2.1 Observation sites and campaigns

Two field campaigns were conducted in this study, including a single-site campaign from 21 August to 14 September 2022 and a two-site campaign from 30 May to 5 June 2023.

The 2022 campaign was conducted at the Shenzhen National Climate Observatory (22°29′08″ N, 114°33′57″ E; Site 1; Fig. S1), a coastal background station on the Dapeng Peninsula (Shenzhen, China) that is distant from major anthropogenic emission sources. Vertical profiles of air pollutants and meteorological parameters were obtained using UAVs to examine the influence of recent air-mass transport pathways on vertical O_3 distributions. VOC measurements were not conducted during this campaign. Further details of the 2022 observations and sampling protocols are provided in Text S2.

The 2023 campaign included coordinated measurements at Site 1 and the Shiyan Meteorological Gradient Observation Tower (22°41′36″ N, 113°54′28″ E; Site 2; Fig. S1), located approximately 70 km from Site 1 within the same city. During this campaign, the Pearl River Delta was affected by the outer circulation of Super Typhoon Mawar from 29 May to 1 June. The observation period was therefore divided into Stage I (30 May–1 June), when the typhoon exerted a stronger influence on the region, and Stage II (2–4 June), when its influence was substantially weaker. At Site 1, UAV measurements provided vertical profiles of O_3, NO_2, CO, $PM_{2.5}$, PM_{10}, VOCs, and meteorological parameters. At Site 2, VOCs were measured continuously near the surface, while O_3, NO_2, and $PM_{2.5}$ were monitored at 0, 60, 110, 210, and 325 m above ground level (AGL). Detailed descriptions of the instrumentation and sampling protocols used during the 2023 campaign are provided in the following sections.

2.2 UAV platforms and sampling protocols

UAV flights were only performed at Site 1. During the 2023 campaign, two UAV platforms were deployed. A hexacopter UAV (DJI M600 Pro) was used for VOC collection, whereas a quadcopter UAV (DJI M300 RTK) was used for high-resolution vertical profiling of other air pollutants and meteorological parameters (Fig. S2).

For VOC measurements, sampling was conducted at 09:00, 15:00, and 21:00 local time each day. Ambient air was collected at 0, 150, 300, and 450 m AGL using Tedlar bags. At each sampling altitude, two 10 L Tedlar bags housed in an acrylic enclosure mounted on the UAV were filled simultaneously. To reduce moisture-related artifacts, the sampled air was passed through calcium chloride. A potassium iodide (KI) scrubber was used to remove O_3 and limit oxidative losses of reactive VOCs (Fick et al., 2001; Mermet et al., 2019). O_3 and humidity can affect VOC measurements, as demonstrated in evaluations of sampling systems and O_3 scrubbers (Ernle et al., 2023). The collected air samples were subsequently transferred to sorbent tubes packed with Tenax TA and Carbograph 5TD at a flow rate of 0.2 L min^{-1} for laboratory analysis. The storage time in the Tedlar bags before transfer was kept below 2 h. Detailed analytical and quality-control procedures are provided in Text S1.

https://doi.org/10.5194/egusphere-2026-6769
Preprint. Discussion started: 20 November 2026
© Author(s) 2026. CC BY 4.0 License.

For the other pollutant gases, vertical profiles of O_x, NO_2, CO, $PM_{2.5}$, and PM_{10} (Table S1), together with wind speed, wind direction, temperature, and relative humidity, were scheduled at 08:00, 09:30, 11:00, 14:00, 15:30, 17:00, 20:00, 21:30, and 23:00 local time whenever weather conditions permitted. Actual flight times varied with field conditions, and the corresponding measurement timestamps were used in the event-specific analyses and figures. Each flight ascended from the surface to approximately 500 m AGL and lasted approximately 30 min. Only measurements collected during the ascent were used in the present analysis. Simultaneous ground-based measurements were conducted for instrument evaluation and calibration.

The 2022 campaign employed a similar vertical-profiling approach using the DJI M300 platform. Vertical profiles of air pollutants and meteorological parameters were obtained at 09:00, 11:00, 14:00, 16:00, 19:00, and 21:00 local time from 21 August to 14 September 2022. VOC measurements were not conducted during the 2022 campaign. Detailed information on the 2022 UAV observations, sampling protocols, and instrument calibration is provided in Text S2.

2.3 Pollutant detection and laboratory chemical analysis

At Site 1, O_x, NO_2, CO, $PM_{2.5}$, and PM_{10} were measured using a multi-sensor package (Sniffer4D V2, Soarability Pte. Ltd.) onboard the DJI M300 UAV (Table S1). O_3 concentrations were derived from the measured O_x and NO_2 signals ($O_3 = O_x - NO_2$). Details of the sensing system have been described elsewhere (Jiang et al., 2024; Li et al., 2025). UAV-based pollutant measurements were calibrated against collocated ground-based reference instruments. Whenever the UAV was not in flight, the sensor package was placed adjacent to the reference instruments to obtain collocated measurements for calibration.

Sensor responses were calibrated using a Random Forest regression model implemented in scikit-learn (Breiman, 2001; Pedregosa et al., 2011). Sensor signals, relative humidity, and temperature were used as predictor variables, with measurements from the corresponding reference instruments serving as training targets. The model consisted of 500 decision trees, with a maximum tree depth of 10 and a minimum of five samples required to split an internal node; all other parameters were set to their default values. Calibration performance was evaluated on the training set (80% of the samples) and the held-out test set (20% of the samples) using the coefficient of determination (R^2), regression slope, root mean square error (RMSE), and mean bias error (MBE). Residuals were calculated as the differences between predicted concentrations and reference measurements. Random Forest predictions are compared with the reference measurements in Fig. S3, and the test-set evaluation metrics and 95% residual intervals are reported in Table S2.

VOCs collected at Site 1 were analyzed offline using thermal desorption–gas chromatography–mass spectrometry (TD-GC-MS; GERSTEL TD3.5+ coupled to an Agilent 7890B GC and 7000D MS). Seventy-seven VOC species spanning alkanes, alkenes, aromatics, oxygenated VOCs, and halocarbons were included in the analyses. Detailed procedures for compound identification, calibration, detection limits, and quality assurance and quality control are provided in Text S1.

At Site 2, VOCs were measured continuously near the surface using an online gas chromatography–mass spectrometry/flame ionization detection system (GC-MS/FID; TH-300B, Wuhan Tianhong Ltd.) based on the system described by Wang et al. (2014). The analytical system covered 116 VOC species, of which 93 passed the study-specific identification and quality-control criteria and were included in the analyses. Light hydrocarbons (C_2 to C_5) were quantified using the FID channel, whereas the remaining VOCs were analyzed using the MS detector. Detailed analytical and quality-control procedures are provided in Text S1.

The VOC species included in the analyses at the two sites and their representation in the Master Chemical Mechanism (MCM) v3.3.1 are summarized in Table S3.

https://doi.org/10.5194/egusphere-2026-6769
Preprint. Discussion started: 20 November 2026
© Author(s) 2026. CC BY 4.0 License.

2.4 Meteorological characterization and air-mass classification

Meteorological conditions during the campaigns were characterized using wind measurements obtained during UAV profiling together with regional air-mass trajectory analysis. UAV-derived wind speed and direction were cross-checked against concurrent ground-based meteorological observations to evaluate their ability to represent local flow conditions (Fig. S4).

Recent regional transport to Site 1 was characterized using 12 h backward trajectories calculated with the Hybrid Single-Particle Lagrangian Integrated Trajectory (HYSPLIT) model driven by 1° Global Data Assimilation System (GDAS1) meteorological fields. Trajectories were initialized at 500 m AGL over Site 1 for both campaigns. For each trajectory, hourly positions from 1 to 12 h before arrival were classified as being over land or ocean using the Natural Earth land mask. The fraction of valid trajectory positions over land was then calculated. Profiles with land fractions greater than 0.5 were classified as land-pathway air masses, those with land fractions lower than 0.5 were classified as marine-pathway air masses, and equal-fraction cases were excluded from the binary comparison. The same trajectory duration, receptor height, land-mask procedure, and pathway-classification criteria were applied to all valid profiles in both campaigns. Full calculation and classification details are provided in Text S3, and the classified profiles are listed in Table S4.

2.5 Model simulation for surface O_3 formation

Surface O_3 chemistry at Sites 1 and 2 was simulated using AtChem2 (https://github.com/AtChem/AtChem2), a zero-dimensional observation-constrained box model (OBM) (Sommariva et al., 2020). Gas-phase chemistry was represented using the Master Chemical Mechanism (MCM v3.3.1) (Saunders et al., 2003; Jenkin et al., 2015). The model was constrained by observations of O_3, CO, NO, NO_2, VOCs, temperature, and relative humidity at each site. At Site 1, VOC measurements obtained at 09:00, 15:00, and 21:00 were linearly interpolated to 1 h resolution before being used as model constraints, whereas continuous VOC measurements at Site 2 were averaged to hourly values. All observational inputs were updated at 1 h intervals.

Because MCM v3.3.1 does not explicitly represent all VOC species included in the analyses, only compounds with corresponding MCM chemistry were used as VOC constraints. Of the available VOC measurements, 55 species at Site 1 and 65 species at Site 2 were represented in MCM v3.3.1. The primary cross-site model comparison used the 44 MCM-represented VOC species available at both sites.

Photochemical production and loss pathways were diagnosed from the OBM outputs. The net photochemical O_3 production rate used in the photochemical budget analysis was calculated as follows.

$$P_{net}(O_3) = P(O_3) - L(O_3)$$

where $P(O_3)$ and $L(O_3)$ describe photochemical production and loss diagnostics that exclude the rapid cycling of O_3, NO, and NO_2. The full O_3 chemical tendency includes all reactions directly producing or consuming O_3, including NO titration and O_3 formation following NO_2 photolysis. The full production and loss rates, $P_{full}(O_3)$ and $L_{full}(O_3)$, are the sums of these reaction rates weighted by their O_3 stoichiometric coefficients. The modeled chemical tendency used for comparison with the observations was calculated as follows.

$$\left(\frac{d[O_3]}{dt}\right)_{chem} = P_{full}(O_3) - L_{full}(O_3)$$

The observed hourly O_3 change rate was calculated from consecutive hourly observations.

$$\left(\frac{d[O_3]}{dt}\right)_{obs} = \frac{[O_3]_{t+\Delta t} - [O_3]_t}{\Delta t}$$

The time interval Δt was 1 h. The full modeled chemical tendency and observed change rate were compared on the same hourly basis. $P_{net}(O_3)$ characterizes net photochemical production, whereas $P_{full}(O_3) - L_{full}(O_3)$ describes the complete

https://doi.org/10.5194/egusphere-2026-6769
Preprint. Discussion started: 20 November 2026
© Author(s) 2026. CC BY 4.0 License.

chemical change in O_3 itself. The modeled chemical increment was obtained by integrating the full chemical tendency over the selected period.

$$\Delta O_{3,chem} = \int_{t_0}^{t_1} (P_{full}(O_3) - L_{full}(O_3))dt$$

The observed O_3 increment was calculated over the same period.

$$\Delta O_{3,obs} = [O_3]_{t_1} - [O_3]_{t_0}$$

The increment not explained by local gas-phase chemistry and its fraction of the observed increase were calculated as follows.

$$\Delta O_{3,unresolved} = \Delta O_{3,obs} - \Delta O_{3,chem}$$

$$f_{unresolved} = \frac{\Delta O_{3,unresolved}}{\Delta O_{3,obs}} \times 100\%$$

This unresolved component may include horizontal and vertical transport, mixing, deposition, dilution, as well as uncertainties in model inputs and chemical mechanisms.

Additional VOC-class sensitivity runs omitted individual classes (oxygenated VOCs, halogenated VOCs, alkanes, alkenes, or aromatics) and compared net O_3 production with the all-included-VOC simulation at each site on 30 May and 4 June 2023.

3. Results

3.1 Regional transport pathways and vertical pollutant distributions

To assess the influence of regional transport on vertical pollutant distributions, we compared UAV profiles obtained at Site 1 under land- and marine-pathway air masses during the 2022 and 2023 campaigns (Fig. 1). The same trajectory-based classification was applied to both campaigns, allowing the vertical distributions of O_3, NO_2, CO, and $PM_{2.5}$ to be compared consistently.

During the 2023 campaign, mean O_3 concentrations in land-pathway air were approximately 170 μg m^{-3} across much of the 0–500 m AGL column, compared with approximately 100 μg m^{-3} in marine-pathway air (Fig. 1A). NO_2, CO, and $PM_{2.5}$ showed clear differences in the same direction. Land-pathway trajectories passed over the Pearl River Delta and inland South China more often, while marine-pathway trajectories approached predominantly from the South China Sea.

The longer 2022 campaign showed a weaker but similar O_3 contrast (Fig. 1B). Land-pathway concentrations were approximately 140 μg m^{-3}, compared with 120 μg m^{-3} in marine-pathway air. NO_2, CO, and $PM_{2.5}$ were also generally higher in land-pathway air, although the differences varied by pollutant.

Similar pathway-dependent differences were therefore observed in both campaigns. The stronger 2023 contrast coincided with warmer conditions and higher VOC abundance during typhoon influence (Sect. 3.2). The 2022 campaign took place in another season and partly overlapped with localized COVID-19 restrictions in Shenzhen, likely reducing emissions in the affected areas. Across the two campaigns, regional transport was an important control on the vertical pollutant environment at Site 1, while the magnitude of its influence varied with the broader emission and synoptic conditions. These measurements provide one of the few vertically resolved, multi-pollutant comparisons of land- and marine-pathway air in the Pearl River Delta, offering a reference for interpreting regional inflow under changing conditions.

https://doi.org/10.5194/egusphere-2026-6769
Preprint. Discussion started: 20 November 2026
© Author(s) 2026. CC BY 4.0 License.

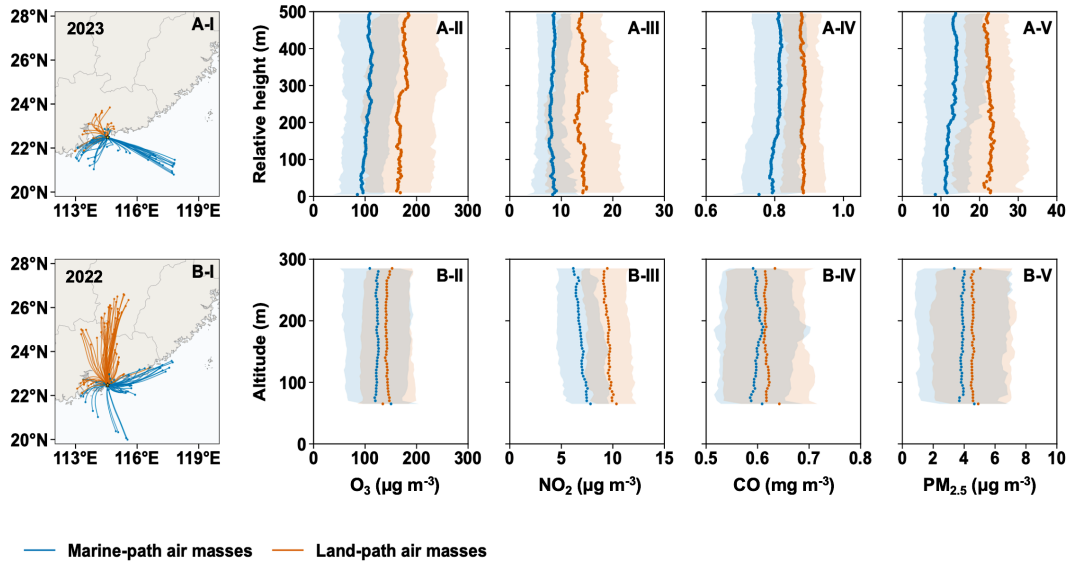


Figure 1. Regional transport pathways and vertical pollutant distributions at Site 1 during the 2023 (A) and 2022 (B) campaigns. Panels A-I and B-I show 12 h HYSPLIT backward trajectories arriving at 500 m AGL. Blue and orange indicate marine-pathway and land-pathway air, respectively. Panels A-II to A-V and B-II to B-V show the corresponding campaign-mean vertical profiles of O_3, NO_2, CO, and $PM_{2.5}$; shading indicates ±1 standard deviation among individual profiles. The profiles extend to 500 m AGL in 2023 and approximately 300 m AGL in 2022. The same trajectory settings and pathway-classification criteria were applied to both campaigns.

3.2 Meteorological and chemical changes under tropical-cyclone influence

Building on the regional transport context identified above, we compared 30 May–1 June 2023 (Stage I), when the outer circulation of Super Typhoon Mawar exerted stronger influence over the region, with 2–4 June 2023 (Stage II), when the tropical-cyclone influence had weakened. The evolving influence of Mawar provided an observational opportunity to examine how concurrent changes in meteorology, photochemistry, and atmospheric transport shaped O_3 evolution.

As shown in Fig. 2A and B, Stage I was characterized by systematically higher temperatures and lower relative humidity than Stage II. The temperature difference persisted throughout the vertical column, indicating that the two stages represented distinctly different meteorological environments and provided different conditions for both photochemical processing and pollutant transport.

Substantial differences were also observed in VOC abundance and composition. Total VOC concentrations during Stage I were approximately 12 to 13 ppb throughout the sampled 0 to 450 m layers, compared with approximately 5 to 6 ppb during Stage II (Fig. 2C and D). Warmer conditions during Stage I could favour emissions of temperature-sensitive VOCs, while changes in regional transport could also modify the abundance and composition of precursors reaching the site.

Multiple VOC classes, including alkanes, alkenes, aromatics, and oxygenated VOCs (OVOCs), contributed to the compositional differences between the two stages (Fig. 2C and D). Specifically, alkenes were dominated by isoprene (Fig. S5) and exhibited higher concentrations near the surface during Stage I, consistent with local biogenic emissions from the surrounding vegetation under warmer conditions. Aromatics, represented mainly by benzene, toluene, ethylbenzene, and

https://doi.org/10.5194/egusphere-2026-6769
Preprint. Discussion started: 20 November 2026
© Author(s) 2026. CC BY 4.0 License.

xylenes (BTEX), showed enhanced concentrations in the upper part of the observed layer during the daytime (Fig. S5), suggesting a greater influence of transported anthropogenic emissions (Song et al., 2024). OVOCs, which can contribute to urban O_3 formation (Huang et al., 2025), also exhibited a pronounced vertical contrast. During Stage I, their concentrations increased from approximately 4 ppb near the surface to about 6 ppb aloft, whereas they remained near 2 ppb at most altitudes during Stage II. The abundance and composition of OVOCs can provide useful indicators of contributions from both primary emissions and secondary photochemical formation. For example, ethyl acetate and acetone (Fig. S5) can have substantial primary contributions, whereas methyl vinyl ketone and methacrolein (Fig. S5) are characteristic products of isoprene oxidation (Lyu et al., 2024). Together, these vertical and compositional differences indicate the combined influences of local biogenic emissions, regional transport, and enhanced photochemical processing during Stage I (see also Sect. 3.4).

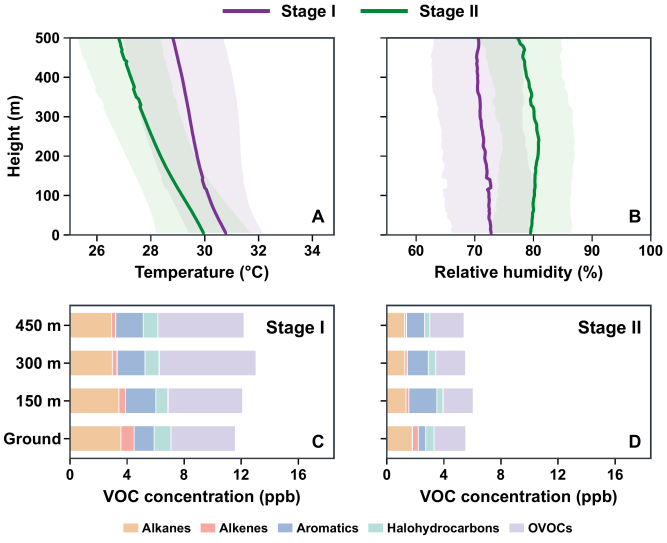


Figure 2. Meteorological conditions and VOC distributions at Site 1 during Stage I and Stage II. Panels A and B show mean vertical profiles of temperature and relative humidity, respectively, with shading indicating ±1 standard deviation. Panels C and D show the concentrations of VOC classes at the surface and 150, 300, and 450 m AGL during Stage I and Stage II, respectively. Stage I covers 30 May–1 June 2023, and Stage II covers 2–4 June 2023.

3.3 Contrasting vertical O_3 evolution at the coastal and inland sites

To examine how these meteorological and chemical conditions were reflected in the vertical O_3 distribution, we compared simultaneous O_3 and wind observations at the coastal and inland sites, focusing first on 30 May during Stage I (Fig. 3).

To quantify the relationship between the evolving wind structure and the vertical O_3 distribution at Site 1, layer means were calculated for the lower (0–150 m AGL) and upper (300–450 m AGL) parts of each profile. The O_3 gradient (ΔO_3) was defined as the upper-minus-lower layer-mean concentration difference, and the wind-direction contrast ($\Delta\theta$) as the minimum circular difference between the corresponding layer-mean wind directions. Pearson correlations paired $\Delta\theta$ with ΔO_3 from either the same profile or the immediately subsequent profile on the same day (Table S5). Because the profiles were unevenly spaced, the subsequent-profile analysis represents the next observation rather than a fixed time lag. Interpolation was used only to display the time–height fields; all gradient and correlation calculations used the original observations.

https://doi.org/10.5194/egusphere-2026-6769
Preprint. Discussion started: 20 November 2026
© Author(s) 2026. CC BY 4.0 License.

At Site 1, O_3 was relatively homogeneous during the morning but subsequently developed a pronounced vertical structure, with elevated concentrations appearing earlier aloft and later at lower altitudes, while wind directions also changed at different heights (Fig. 3A-I and B-I). During the morning, near-surface winds were predominantly around 100°, indicating onshore flow from the adjacent marine sector (Fig. S1), whereas markedly different wind directions occurred aloft. The directional difference between the lower and upper layers reached approximately 180°, producing an almost complete reversal of wind direction with altitude. This combination of onshore near-surface flow and opposing flow aloft is characteristic of the vertical circulation associated with a sea breeze. The vertical wind-direction difference subsequently decreased rapidly during the day, while the upper-minus-lower O_3 difference continued to increase toward its maximum (Fig. 3B-I and C-I). The O_3 gradient then weakened and eventually reversed at night.

Similar temporal behaviour occurred on 31 May and 1 June during Stage I (Fig. S6). On all three days, the relationship between the vertical wind-direction contrast and the O_3 gradient at the subsequent profile was stronger than the corresponding same-profile relationship (Table S5). Pearson *r* increased from 0.32 to 0.66 on 30 May, from 0.42 to 0.51 on 31 May, and from 0.51 to 0.82 on 1 June when the O_3 gradient at the subsequent profile was considered. These consistent relationships between the vertical wind-direction contrast and the O_3 gradient suggest that changes in the vertical wind structure likely contributed to the subsequent evolution of the vertical O_3 distribution. The delayed O_3 response may reflect the combined influence of multiple processes operating over different timescales, including advection, vertical mixing, and exchange among air masses with different chemical histories.

The close association between O_3 increases and height-dependent wind shifts highlights the importance of the evolving land–sea-breeze circulation and its interaction with regional flow in shaping coastal O_3 evolution. Changes in near-surface coastal winds and regional flow aloft can alter air-mass influence at different heights, exposing different parts of the sampled column to air masses with distinct transport and chemical histories. The resulting vertical O_3 structure therefore reflects the transport and redistribution associated with these wind shifts, while vertical mixing and local chemical production and loss further modify the magnitude and persistence of the observed O_3 gradients.

By contrast, Site 2 exhibited a persistent higher O_3 concentration aloft. On 30 May, O_3 remained substantially higher at 325 m than near the surface throughout the observation period (Fig. 3A-II and C-II). This persistent enhancement aloft was also observed on 31 May and 1 June (Fig. S6), indicating that the vertical structure recurred throughout Stage I rather than being unique to a single day. Located farther inland than Site 1, Site 2 is less directly influenced by local coastal thermal circulations and exhibited comparatively coherent wind directions through much of the tower layer during the daytime, without the pronounced height-dependent transitions observed at Site 1 (Fig. 3B-II). The persistent enhancement aloft is a result of stronger regional or elevated-layer O_3 influence combined with greater O_3 loss near the surface. Site 2 is surrounded largely by forest and reservoir areas with limited nearby anthropogenic precursor emissions, and surface deposition together with reactions involving reactive biogenic VOCs may contribute to near-surface O_3 loss.

Together, the two sites demonstrate that nearby coastal and inland environments within the same city can exhibit distinctly different vertical O_3 responses. At Site 1, O_3 gradients changed as coastal and regional flows shifted at different heights, whereas Site 2 maintained higher O_3 aloft under comparatively coherent daytime winds. The simultaneous wind observations therefore help explain why the two sites developed different vertical O_3 structures under the same regional weather conditions.

https://doi.org/10.5194/egusphere-2026-6769
Preprint. Discussion started: 20 November 2026
© Author(s) 2026. CC BY 4.0 License.

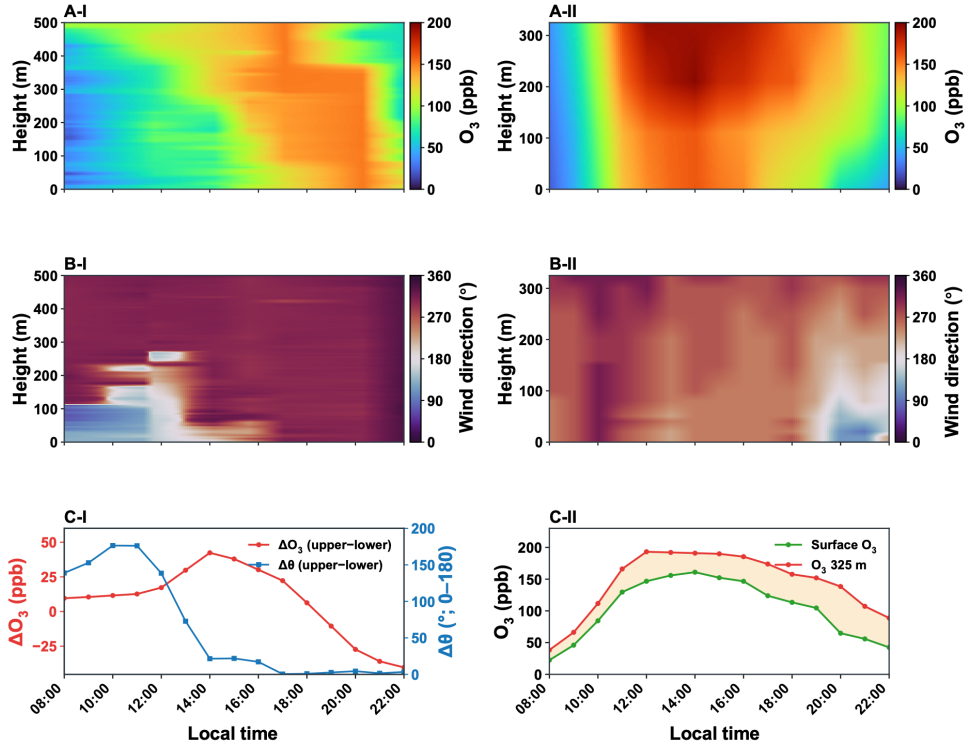


Figure 3. Vertical O_3 and wind evolution on 30 May 2023. (A-I, A-II) O_3 at Sites 1 and 2 on a common 0–200 ppb scale. (B-I, B-II) Wind direction. (C-I) Site 1 upper-minus-lower layer-mean O_3 difference (ΔO_3) and minimum circular wind-direction difference ($\Delta\theta$) between 300–450 and 0–150 m AGL. (C-II) Site 2 O_3 near the surface and at 325 m. Data in panels A and B were interpolated to 10-min intervals, while those in panel C were interpolated to 1-h intervals for visualization. Quantitative gradient and correlation analyses use original observations. O_3 mass concentrations were converted to ppb at standard temperature and pressure.

3.4 Local photochemical contributions and physical controls on O_3 evolution

We next used observation-based modelling to quantify the contribution of local gas-phase chemistry to near-surface O_3 evolution and to assess its sensitivity to precursor reductions at the two sites.

Net photochemical O_3 production was substantially stronger during Stage I than during Stage II at both sites (Fig. 4A-I, A-II, B-I, and B-II). This result is consistent with the warmer conditions and higher VOC abundance during the period of stronger typhoon influence. To assess how this enhanced photochemistry contributed to the observed increases, we compared the hourly observed O_3 change rate with the OBM-resolved local chemical O_3 tendency (Fig. 4A-III, A-IV, B-III, and B-IV).

At Site 1, observed O_3 increased by approximately 79 ppb between 14:00 and 18:00 local time on 30 May, whereas the cumulative O_3 change represented by local gas-phase chemistry was approximately 47 ppb. Local chemistry therefore accounted for approximately 59% of the observed increase. The remaining 32 ppb, or 41%, coincided with the rapid changes in vertical O_3 and wind structure shown in Fig. 3, supporting an important role for physical redistribution alongside local production.

https://doi.org/10.5194/egusphere-2026-6769
Preprint. Discussion started: 20 November 2026
© Author(s) 2026. CC BY 4.0 License.

At Site 2, local chemistry accounted for a smaller fraction of the rapid surface O_3 increase. Between 09:00 and 13:00 local time on 30 May, observed O_3 increased by approximately 118 ppb, whereas the cumulative increase represented by local chemistry was only about 39 ppb. Local chemistry accounted for approximately 33% of the observed increase, leaving 79 ppb, or 67%, beyond the local chemical contribution. Together with the persistent enhancement of O_3 at 325 m documented in Sect. 3.3, this result indicates that local photochemical production alone was insufficient to explain the rapid increase in surface O_3 at Site 2. The persistent enhancement aloft, together with the rapid surface O_3 increase, points to important contributions from regional advection and exchange with O_3-rich air aloft. During Stage II, both observed and OBM-resolved O_3 change rates were comparatively small at both sites (Fig. 4A-IV and B-IV), consistent with the weaker photochemical activity during this period.

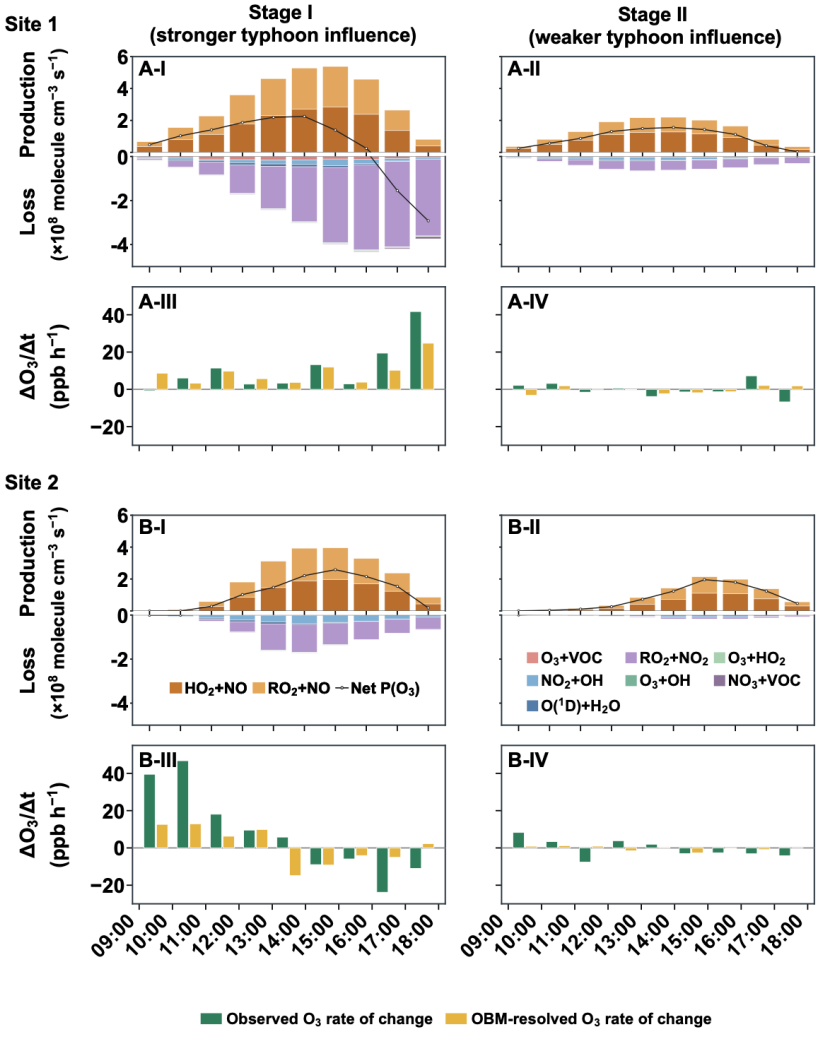


Figure 4. Photochemical O_3 production and loss rates and hourly O_3 change rates at Site 1 (A) and Site 2 (B). Panels I and III show results for 30 May 2023 (Stage I), whereas panels II and IV show results for 4 June 2023 (Stage II). The upper panels show the contributions of individual photochemical production and loss pathways and the resulting

https://doi.org/10.5194/egusphere-2026-6769
Preprint. Discussion started: 20 November 2026
© Author(s) 2026. CC BY 4.0 License.

net O_3 production rate. The lower panels compare the observed hourly O_3 change rate with the O_3 tendency resolved by the observation-based model from gas-phase reactions that directly produce or consume O_3.

These results illustrate two related aspects of vertical O_3 evolution. In the absence of pronounced perturbations from local circulation or wind shifts, large concentration contrasts can persist between the surface and the air aloft. Changes in coastal circulation or wind structure can disturb this stratification and redistribute O_3 vertically, thereby altering surface concentrations without an equivalent increase in local chemical production. These processes could be directly identified only because simultaneous vertically resolved observations were available; surface measurements alone would not distinguish locally produced O_3 from O_3 supplied through transport and vertical exchange. Resolving this distinction is important for interpreting surface O_3 evolution and for designing control strategies that appropriately balance local precursor reductions with regional emission controls.

We then examined how VOC composition affected local O_3 production at the two sites. The primary cross-site model comparison used the 44 MCM-represented VOCs common to both datasets. We further tested whether differences in VOC species coverage affected the model results. Sensitivity simulations using the full set of MCM-represented VOCs available at each site produced similar O_3 production and loss rates and OBM-resolved O_3 tendencies, indicating that differences in VOC coverage did not materially affect the cross-site comparison. The VOC-class sensitivity calculations showed that local O_3 production at both sites remained responsive to reductions in VOC precursors, although the relative importance of individual VOC classes differed between the two environments (Fig. S7). At Site 1, alkenes exerted the strongest influence on modelled local O_3 production. At Site 2, the sensitivity was more broadly distributed, with reductions in alkenes, aromatics, and OVOCs producing the largest effects.

The vertical observations and model calculations demonstrate that enhanced photochemistry and physical redistribution acted concurrently. Local gas-phase chemistry contributed substantially to O_3 formation at both sites, but processes beyond local chemistry were required to account for the magnitude and timing of the rapid observed O_3 increases.

4. Conclusions and implications

This study combined UAV profiles, tower observations, air-mass trajectories, and observation-based atmospheric chemistry modelling to investigate O_3 evolution at coastal and inland sites within the same city. During the period of stronger typhoon influence, warmer and drier conditions, higher VOC concentrations, and enhanced local photochemical activity occurred together with pronounced changes in atmospheric transport and vertical wind structure. Nevertheless, the two sites exhibited distinct O_3 evolution. At the coastal site, height-dependent wind shifts accompanied the development and subsequent reversal of the vertical O_3 gradient, indicating that interactions between coastal circulation and regional flow affected O_3 redistribution. At the inland site, O_3 remained consistently higher aloft while near-surface concentrations increased rapidly, indicating sustained exchange with O_3-rich air above the surface.

The OBM analysis showed that local gas-phase chemistry accounted for approximately 59% and 33% of the observed rapid O_3 increases at the coastal and inland sites, respectively. Regional transport and vertical redistribution therefore made substantial contributions that differed between the two environments. VOC-reduction simulations nevertheless suppressed local O_3 production at both sites. Alkenes exerted the strongest influence at the coastal site, whereas alkenes, aromatics, and OVOCs were all important at the inland site.

These findings have direct implications for O_3 mitigation. Local VOC controls remain important for reducing in situ O_3 production, but their effectiveness in lowering ambient concentrations may depend on the concurrent transport environment.

https://doi.org/10.5194/egusphere-2026-6769
Preprint. Discussion started: 20 November 2026
© Author(s) 2026. CC BY 4.0 License.

During periods when O_3 or its precursors are strongly affected by regional inflow or exchange with elevated layers, local measures may need to be complemented by coordinated precursor reductions over a broader spatial scale. The differences in VOC sensitivity between the two sites also indicate that control priorities should account for local precursor composition rather than applying a uniform strategy across an entire metropolitan region.

The results also demonstrate the importance of vertically resolved observations for O_3 monitoring and episode diagnosis. Surface measurements alone cannot reliably distinguish locally produced O_3 from O_3 supplied through regional transport or vertical redistribution. At the coastal site, the apparent downward progression of enhanced O_3 could not be interpreted simply as direct downward transport once the evolving vertical wind field was considered. At the inland site, the persistent elevated O_3 layer would not have been apparent from surface observations alone. Combining routine surface monitoring with vertically resolved chemical and meteorological measurements would improve the identification of the processes driving individual O_3 episodes and help determine whether local or regionally coordinated controls are required.

Tropical cyclones are recurrent meteorological disturbances in tropical and subtropical coastal regions. As the climate warms, the proportion of intense tropical cyclones, their peak wind speeds, and associated precipitation are projected to increase (IPCC, 2021). Understanding their effects on O_3 pollution is therefore increasingly important for densely populated coastal regions. Because tropical cyclones can alter atmospheric chemistry and transport simultaneously, the relative effectiveness of local and regional O_3 controls may vary among events, locations, and stages of storm evolution. Identifying the appropriate spatial scale for mitigation therefore requires photochemical production and three-dimensional transport to be diagnosed together, particularly under rapidly evolving synoptic conditions.

https://doi.org/10.5194/egusphere-2026-6769
Preprint. Discussion started: 20 November 2026
© Author(s) 2026. CC BY 4.0 License.

Supporting Information. The supporting information includes the following items:

Text S1 VOC chemical analysis and quality assurance and quality control.

Text S2 UAV observations during the 2022 field campaign.

Text S3 Backward-trajectory calculation and air-mass pathway classification.

Table S1 Summary of instruments used for UAV observations and ground-based measurements.

Table S2 Random Forest calibration performance and residual-based uncertainty metrics for UAV pollutant measurements during the 2023 campaign.

Table S3 VOC species included in the analyses at Sites 1 and 2 and their representation in the MCM.

Table S4 Summary of UAV profiles and air-mass classifications during the 2022 and 2023 campaigns.

Table S5 Same-profile and one-profile-lag relationships between vertical wind-direction contrast and O_3 gradient at Site 1 during the three Stage I days.

Figure S1 Locations of observation sites.

Figure S2 UAV platforms used for vertical pollutant profiling and VOC sampling.

Figure S3 Comparison of Random Forest-predicted and reference-instrument pollutant concentrations during the 2023 campaign.

Figure S4 Comparison of wind direction measured by the UAV and ground-based reference instrument.

Figure S5 Vertical distributions of selected VOC species at Site 1 during Stage I and Stage II.

Figure S6 Vertical O_3 evolution and wind-direction structures at Sites 1 and 2 on 31 May and 1 June 2023 during Stage I.

Figure S7 Sensitivity of surface net O_3 production to changes in VOC composition at Sites 1 and 2.

Corresponding Author. Jianhuai Ye (yejh@sustech.edu.cn), ORCID: 0000-0002-9063-3260

Data availability. All data are available in the main text or Supplement. Additional relevant data can be obtained from the corresponding author upon request.

Author contribution. J.Y. designed the research; D.N., X.H., and Shaojie Jiang conducted UAV sampling in the 2022 summer campaign; X.H., W.Z., Y.W., Y.Y., and J.Y. conducted UAV sampling in the 2023 summer campaign; W.Z., Y.W., and Shaojie Jiang performed the chemical analyses; Shaojie Jiang, X.G., and J.Y. analyzed the data and prepared the original manuscript; Shaojie Jiang, X.G., D.N., X.H., W.Z., H.Y., Y.W., Y.Y., W.S., L.M., T.C., Y.Z., Shutong Jiang, Q.W., J.W., C.L., L.Z., Z.Z., T.-M.F., X.Y., and J.Y. contributed to data interpretation and manuscript revision.

Competing interests. The authors declare that they have no conflict of interest.

Financial support. This work was funded by the National Key Research and Development Program of China (grant no. 2024YFC3714300), the Jing-Jin-Ji Regional Integrated Environmental Improvement–National Science and Technology Major Project (no. 2026ZD1209500), the National Natural Science Foundation of China (nos. 42375091 and U24A20515), and the Shenzhen Science and Technology Program (nos. JCYJ20241202152804007, KQTD20240729102048052, and JCYJ20230807151059005). Support from the Fundamental and Interdisciplinary Disciplines Breakthrough Plan of the

https://doi.org/10.5194/egusphere-2026-6769
Preprint. Discussion started: 20 November 2026
© Author(s) 2026. CC BY 4.0 License.



Ministry of Education of China (JYB2025XDXM909) and the High Level of Special Funds from Southern University of Science and Technology (G03050K001) is gratefully acknowledged.

https://doi.org/10.5194/egusphere-2026-6769
Preprint. Discussion started: 20 November 2026
© Author(s) 2026. CC BY 4.0 License.

References

Batista, C. E., Ye, J., Ribeiro, I. O., Guimarães, P. C., Medeiros, A. S. S., Barbosa, R. G., Oliveira, R. L., Duvoisin, S., Jardine, K. J., Gu, D., Guenther, A. B., McKinney, K. A., Martins, L. D., Souza, R. A. F., and Martin, S. T.: Intermediate-scale horizontal isoprene concentrations in the near-canopy forest atmosphere and implications for emission heterogeneity, Proc. Natl. Acad. Sci. USA, 116, 19318–19323, https://doi.org/10.1073/pnas.1904154116, 2019.

Breiman, L.: Random forests, Mach. Learn., 45, 5–32, https://doi.org/10.1023/a:1010933404324, 2001.

Chen, D., Su, W., Jiang, S., Yang, H., Zhang, C., Jiang, S., Chang, D., Liang, Y., Wang, H., Yang, X., Fu, T.-M., Zeng, Z., Zhu, L., Shen, H., Wang, C., and Ye, J.: Wind estimation based on flight dynamics of unmanned aerial vehicle: influencing variables and its environmental application, Atmos. Chem. Phys., 26, 3607–3620, https://doi.org/10.5194/acp-26-3607-2026, 2026.

Deng, T., Wang, T., Wang, S., Zou, Y., Yin, C., Li, F., Liu, L., Wang, N., Song, L., Wu, C., and Wu, D.: Impact of typhoon periphery on high ozone and high aerosol pollution in the Pearl River Delta region, Sci. Total Environ., 668, 617–630, https://doi.org/10.1016/j.scitotenv.2019.02.450, 2019.

Ernle, L., Ringsdorf, M. A., and Williams, J.: Influence of ozone and humidity on PTR-MS and GC-MS VOC measurements with and without a $Na_2S_2O_3$ ozone scrubber, Atmos. Meas. Tech., 16, 1179–1194, https://doi.org/10.5194/amt-16-1179-2023, 2023.

Fick, J., Pommer, L., Andersson, B., and Nilsson, C.: Ozone removal in the sampling of parts per billion levels of terpenoid compounds: an evaluation of different scrubber materials, Environ. Sci. Technol., 35, 1458–1462, https://doi.org/10.1021/es0001456, 2001.

Guimarães, P., Ye, J., Batista, C., Barbosa, R., Ribeiro, I., Medeiros, A., Zhao, T., Hwang, W.-C., Hung, H.-M., Souza, R., and Martin, S. T.: Vertical profiles of atmospheric species concentrations and nighttime boundary layer structure in the dry season over an urban environment in Central Amazon collected by an unmanned aerial vehicle, Atmosphere, 11, 1371, https://doi.org/10.3390/atmos11121371, 2020.

He, Z., Wang, X., Ling, Z., Zhao, J., Guo, H., Shao, M., and Wang, Z.: Contributions of different anthropogenic volatile organic compound sources to ozone formation at a receptor site in the Pearl River Delta region and its policy implications, Atmos. Chem. Phys., 19, 8801–8816, https://doi.org/10.5194/acp-19-8801-2019, 2019.

Hu, Q., Ji, X., Hong, Q., Li, J., Li, Q., Ou, J., Liu, H., Xing, C., Tan, W., Chen, J., Chang, B., and Liu, C.: Vertical evolution of ozone formation sensitivity based on synchronous vertical observations of ozone and proxies for its precursors: implications for ozone pollution prevention strategies, Environ. Sci. Technol., 58, 4291–4301, https://doi.org/10.1021/acs.est.4c00637, 2024.

Hu, W., Liu, R., Chen, Z., Ouyang, S., Hu, T., Wang, Y., Cui, Z., Jiang, B., Chen, D., and Liu, S. C.: Processes conducive to high ozone formation in Pearl River Delta in the presence of Pacific tropical cyclones, Atmos. Environ., 307, 119859, https://doi.org/10.1016/j.atmosenv.2023.119859, 2023.

Huang, J., Fung, J. C. H., Lau, A. K. H., and Qin, Y.: Numerical simulation and process analysis of typhoon-related ozone episodes in Hong Kong, J. Geophys. Res. Atmos., 110, D05301, https://doi.org/10.1029/2004JD004914, 2005.

Huang, X., Zheng, W., Li, Y., Li, C., Li, Y., Zhang, N., Pan, C., Lei, Y., Li, H., Zhang, Y., Qin, Y., Zheng, Y., Fu, T.-M., Yang, X., Ge, X., Zhang, H., and Ye, J.: Ozone formation in a representative urban environment: model discrepancies and critical roles of oxygenated volatile organic compounds, Environ. Sci. Technol. Lett., 12, 297–304, https://doi.org/10.1021/acs.estlett.4c01026, 2025.

https://doi.org/10.5194/egusphere-2026-6769
Preprint. Discussion started: 20 November 2026
© Author(s) 2026. CC BY 4.0 License.

IPCC: Climate Change 2021: The Physical Science Basis, Contribution of Working Group I to the Sixth Assessment Report of the Intergovernmental Panel on Climate Change, edited by: Masson-Delmotte, V., Zhai, P., Pirani, A., Connors, S. L., Péan, C., Berger, S., Caud, N., Chen, Y., Goldfarb, L., Gomis, M. I., Huang, M., Leitzell, K., Lonnoy, E., Matthews, J. B. R., Maycock, T. K., Waterfield, T., Yelekçi, O., Yu, R., and Zhou, B., Cambridge University Press, Cambridge, UK and New York, NY, USA, 2391 pp., https://doi.org/10.1017/9781009157896, 2021.

Jenkin, M. E., Young, J. C., and Rickard, A. R.: The MCM v3.3.1 degradation scheme for isoprene, Atmos. Chem. Phys., 15, 11433–11459, https://doi.org/10.5194/acp-15-11433-2015, 2015.

Jiang, S., Wang, Y., Huang, X., Liu, B., Nie, D., Ge, Y., Ma, L., Wang, Q., Wang, J., Ma, Y., Jiang, S., Shu, Z., Zhang, Y., Sun, J., Wu, C., Ge, X., Zhu, L., Shen, H., Wang, C., Zheng, Y., Fu, T.-M., Yang, X., Li, Y. J., Chen, Q., and Ye, J.: Characteristics of nocturnal boundary layer over a subtropical forest: implications for the dispersion and fate of atmospheric species, Environ. Sci. Technol., 58, 23075–23087, https://doi.org/10.1021/acs.est.4c05051, 2024.

Jiang, S., Ge, X., Nie, D., Huang, X., Zheng, W., Yang, H., Wang, Y., Yang, Y., Su, W., Ma, L., Chen, T., Zhang, Y., Jiang, S., Wang, Q., Wang, J., Liu, C., Zhu, L., Zeng, Z., Fu, T.-M., Yang, X., and Ye, J.: Contrasting vertical ozone evolution under typhoon-influenced photochemistry and transport, Zenodo [data set], https://doi.org/10.5281/zenodo.23055771, 2026.

Jiang, Y. C., Zhao, T. L., Liu, J., Xu, X. D., Tan, C. H., Cheng, X. H., Bi, X. Y., Gan, J. B., You, J. F., and Zhao, S. Z.: Why does surface ozone peak before a typhoon landing in southeast China?, Atmos. Chem. Phys., 15, 13331–13338, https://doi.org/10.5194/acp-15-13331-2015, 2015.

Li, K., Jacob, D. J., Shen, L., Lu, X., De Smedt, I., and Liao, H.: Increases in surface ozone pollution in China from 2013 to 2019: anthropogenic and meteorological influences, Atmos. Chem. Phys., 20, 11423–11433, https://doi.org/10.5194/acp-20-11423-2020, 2020.

Li, Y., Zhao, X., Deng, X., and Gao, J.: The impact of peripheral circulation characteristics of typhoon on sustained ozone episodes over the Pearl River Delta region, China, Atmos. Chem. Phys., 22, 3861–3873, https://doi.org/10.5194/acp-22-3861-2022, 2022.

Li, Y., Zhang, C., Su, W., Jiang, S., Nie, D., Wang, Y., Wang, Y., He, H., Chen, Q., Martin, S. T., and Ye, J.: Copter-type UAV-based sensing in atmospheric chemistry: recent advances, applications, and future perspectives, Environ. Sci. Technol., 59, 13532–13550, https://doi.org/10.1021/acs.est.5c00074, 2025.

Liao, Z., Gao, M., Zhang, J., Sun, J., Quan, J., Jia, X., Pan, Y., and Fan, S.: Mixing-layer-height-referenced ozone vertical distribution in the lower troposphere of Chinese megacities: stratification, classification, and meteorological and photochemical mechanisms, Atmos. Chem. Phys., 24, 3541–3557, https://doi.org/10.5194/acp-24-3541-2024, 2024.

Lin, C., Leung, K. K., Yu, A. L., Tsang, R. C., Tsui, W. B., Fung, J. C., Ng, E. K., Cheung, S., Tang, A. W., Ning, Z., Li, Y., Zhang, T., and Lau, A. K.: Effects of synoptic patterns on the vertical structure of ozone in Hong Kong using lidar measurement, Atmos. Environ., 257, 118490, https://doi.org/10.1016/j.atmosenv.2021.118490, 2021.

Liu, X., Huang, Y., Chen, Y., Feng, X., Li, J., Xu, Y., Chen, Y., Gu, D., Sun, H., Ning, Z., Yu, J., Chow, W. S., Lin, C., Xiang, Y., Zhang, T., Granier, C., Brasseur, G., Wang, Z., and Fung, J. C. H.: Abundance of volatile organic compounds and their role in ozone pollution management: evidence from multi-platform observations and model representation during the 2021–2022 field campaign in Hong Kong, Atmos. Chem. Phys., 25, 17629–17649, https://doi.org/10.5194/acp-25-17629-2025, 2025.

https://doi.org/10.5194/egusphere-2026-6769
Preprint. Discussion started: 20 November 2026
© Author(s) 2026. CC BY 4.0 License.



Lu, X., Zhang, L., Wang, X., Gao, M., Li, K., Zhang, Y., Yue, X., and Zhang, Y.: Rapid increases in warm-season surface ozone and resulting health impact in China since 2013, Environ. Sci. Technol. Lett., 7, 240–247, https://doi.org/10.1021/acs.estlett.0c00171, 2020.

Lyu, X., Li, H., Lee, S.-C., Xiong, E., Guo, H., Wang, T., and de Gouw, J.: Significant biogenic source of oxygenated volatile organic compounds and the impacts on photochemistry at a regional background site in South China, Environ. Sci. Technol., 58, 20081–20090, https://doi.org/10.1021/acs.est.4c05656, 2024.

Ma, Y., Ye, J., Ribeiro, I. O., Vilà-Guerau de Arellano, J., Xin, J., Zhang, W., Souza, R. A. F., and Martin, S. T.: Optimization and representativeness of atmospheric chemical sampling by hovering unmanned aerial vehicles over tropical forests, Earth Space Sci., 8, e2020EA001335, https://doi.org/10.1029/2020ea001335, 2021.

Mermet, K., Sauvage, S., Dusanter, S., Salameh, T., Léonardis, T., Flaud, P.-M., Perraudin, É., Villenave, É., and Locoge, N.: Optimization of a gas chromatographic unit for measuring biogenic volatile organic compounds in ambient air, Atmos. Meas. Tech., 12, 6153–6171, https://doi.org/10.5194/amt-12-6153-2019, 2019.

Monks, P. S., Archibald, A. T., Colette, A., Cooper, O., Coyle, M., Derwent, R., Fowler, D., Granier, C., Law, K. S., Mills, G. E., Stevenson, D. S., Tarasova, O., Thouret, V., von Schneidemesser, E., Sommariva, R., Wild, O., and Williams, M. L.: Tropospheric ozone and its precursors from the urban to the global scale from air quality to short-lived climate forcer, Atmos. Chem. Phys., 15, 8889–8973, https://doi.org/10.5194/acp-15-8889-2015, 2015.

Ning, Y., Wang, X., Yu, Q., Liang, D., and Zhai, J.: Rapid damage prediction and risk assessment for tropical cyclones at a fine grid in Guangdong Province, South China, Int. J. Disaster Risk Sci., 14, 237–252, https://doi.org/10.1007/s13753-023-00485-y, 2023.

Ouyang, S., Deng, T., Liu, R., Chen, J., He, G., Leung, J. C.-H., Wang, N., and Liu, S. C.: Impact of a subtropical high and a typhoon on a severe ozone pollution episode in the Pearl River Delta, China, Atmos. Chem. Phys., 22, 10751–10767, https://doi.org/10.5194/acp-22-10751-2022, 2022.

Pedregosa, F., Varoquaux, G., Gramfort, A., Michel, V., Thirion, B., Grisel, O., Blondel, M., Prettenhofer, P., Weiss, R., Dubourg, V., Vanderplas, J., Passos, A., Cournapeau, D., Brucher, M., Perrot, M., and Duchesnay, É.: Scikit-learn: machine learning in Python, J. Mach. Learn. Res., 12, 2825–2830, 2011.

Qi, C., Wang, P., Yang, Y., Li, H., Zhang, H., Ren, L., Jin, X., Zhan, C., Tang, J., and Liao, H.: Impacts of tropical cyclone–heat wave compound events on surface ozone in eastern China: comparison between the Yangtze River and Pearl River deltas, Atmos. Chem. Phys., 24, 11775–11789, https://doi.org/10.5194/acp-24-11775-2024, 2024.

Saunders, S. M., Jenkin, M. E., Derwent, R. G., and Pilling, M. J.: Protocol for the development of the Master Chemical Mechanism, MCM v3 (Part A): tropospheric degradation of non-aromatic volatile organic compounds, Atmos. Chem. Phys., 3, 161–180, https://doi.org/10.5194/acp-3-161-2003, 2003.

Shao, M., Zhang, Y., Zeng, L., Tang, X., Zhang, J., Zhong, L., and Wang, B.: Ground-level ozone in the Pearl River Delta and the roles of VOC and NO_x in its production, J. Environ. Manage., 90, 512–518, https://doi.org/10.1016/j.jenvman.2007.12.008, 2009.

Sommariva, R., Cox, S., Martin, C., Borońska, K., Young, J., Jimack, P. K., Pilling, M. J., Matthaios, V. N., Nelson, B. S., Newland, M. J., Panagi, M., Bloss, W. J., Monks, P. S., and Rickard, A. R.: AtChem (version 1), an open-source box model for the Master Chemical Mechanism, Geosci. Model Dev., 13, 169–183, https://doi.org/10.5194/gmd-13-169-2020, 2020.

https://doi.org/10.5194/egusphere-2026-6769
Preprint. Discussion started: 20 November 2026
© Author(s) 2026. CC BY 4.0 License.



Song, X., Li, X.-B., Yuan, B., He, X., Chen, Y., Wang, S., Huangfu, Y., Peng, Y., Zhang, C., Liu, A., Yang, H., Liu, C., Li, J., and Shao, M.: Elucidating key factors in regulating budgets of ozone and its precursors in atmospheric boundary layer, npj Clim. Atmos. Sci., 7, 262, https://doi.org/10.1038/s41612-024-00818-8, 2024.

Wang, J., Wang, P., Tian, C., Gao, M., Cheng, T., and Mei, W.: Consecutive northward super typhoons induced extreme ozone pollution events in eastern China, npj Clim. Atmos. Sci., 7, 244, https://doi.org/10.1038/s41612-024-00786-z, 2024.

Wang, M., Zeng, L., Lu, S., Shao, M., Liu, X., Yu, X., Chen, W., Yuan, B., Zhang, Q., Hu, M., and Zhang, Z.: Development and validation of a cryogen-free automatic gas chromatograph system (GC-MS/FID) for online measurements of volatile organic compounds, Anal. Methods, 6, 9424–9434, https://doi.org/10.1039/c4ay01855a, 2014.

Wang, N., Huang, X., Xu, J., Wang, T., Tan, Z.-M., and Ding, A.: Typhoon-boosted biogenic emission aggravates cross-regional ozone pollution in China, Sci. Adv., 8, eabl6166, https://doi.org/10.1126/sciadv.abl6166, 2022.

Wang, W., Parrish, D. D., Wang, S., Bao, F., Ni, R., Li, X., Yang, S., Wang, H., Cheng, Y., and Su, H.: Long-term trend of ozone pollution in China during 2014–2020: distinct seasonal and spatial characteristics and ozone sensitivity, Atmos. Chem. Phys., 22, 8935–8949, https://doi.org/10.5194/acp-22-8935-2022, 2022.

Wang, X., Zhang, Y., Hu, Y., Zhou, W., Lu, K., Zhong, L., Zeng, L., Shao, M., Hu, M., and Russell, A. G.: Process analysis and sensitivity study of regional ozone formation over the Pearl River Delta, China, during the PRIDE-PRD2004 campaign using the Community Multiscale Air Quality modeling system, Atmos. Chem. Phys., 10, 4423–4437, https://doi.org/10.5194/acp-10-4423-2010, 2010.

Wu, C., Liu, B., Wu, D., Yang, H., Mao, X., Tan, J., Liang, Y., Sun, J. Y., Xia, R., Sun, J., He, G., Li, M., Deng, T., Zhou, Z., and Li, Y. J.: Vertical profiling of black carbon and ozone using a multicopter unmanned aerial vehicle (UAV) in urban Shenzhen of South China, Sci. Total Environ., 801, 149689, https://doi.org/10.1016/j.scitotenv.2021.149689, 2021.

Xue, L., Gu, R., Wang, T., Wang, X., Saunders, S., Blake, D., Louie, P. K. K., Luk, C. W. Y., Simpson, I., Xu, Z., Wang, Z., Gao, Y., Lee, S., Mellouki, A., and Wang, W.: Oxidative capacity and radical chemistry in the polluted atmosphere of Hong Kong and Pearl River Delta region: analysis of a severe photochemical smog episode, Atmos. Chem. Phys., 16, 9891–9903, https://doi.org/10.5194/acp-16-9891-2016, 2016.

Yang, J. X., Lau, A. K. H., Fung, J. C. H., Zhou, W., and Wenig, M.: An air pollution episode and its formation mechanism during the tropical cyclone Nuri's landfall in a coastal city of South China, Atmos. Environ., 54, 746–753, https://doi.org/10.1016/j.atmosenv.2011.12.023, 2012.

Ye, J., Batista, C. E., Guimarães, P. C., Ribeiro, I. O., Vidoudez, C., Barbosa, R. G., Oliveira, R. L., Ma, Y., Jardine, K. J., Surratt, J. D., Guenther, A. B., Souza, R. A. F., and Martin, S. T.: Near-canopy horizontal concentration heterogeneity of semivolatile oxygenated organic compounds and implications for 2-methyltetrols primary emissions, Environ. Sci.: Atmos., 1, 8–20, https://doi.org/10.1039/d0ea00006j, 2021.

Ye, J., Batista, C. E., Zhao, T., Campos, J., Ma, Y., Guimarães, P., Ribeiro, I. O., Medeiros, A. S. S., Stewart, M. P., Vilà-Guerau de Arellano, J., Guenther, A. B., Souza, R. A. F., and Martin, S. T.: River winds and transport of forest volatiles in the Amazonian riparian ecoregion, Environ. Sci. Technol., 56, 12667–12677, https://doi.org/10.1021/acs.est.1c08460, 2022.

Zheng, J., Shao, M., Che, W., Zhang, L., Zhong, L., Zhang, Y., and Streets, D.: Speciated VOC emission inventory and spatial patterns of ozone formation potential in the Pearl River Delta, China, Environ. Sci. Technol., 43, 8580–8586, https://doi.org/10.1021/es901688e, 2009.